




Article

Numerical Simulation and Experimental Validation of the Cladding Material Distribution of Hybrid Semi-Finished Products Produced by Deposition Welding and Cross-Wedge Rolling

Jens Kruse ^{1,*}, Maximilian Mildebrath ², Laura Budde ³, Timm Coors ⁴ ,
Mohamad Yusuf Faqiri ², Alexander Barroi ³ , Malte Stonis ¹, Thomas Hassel ², Florian Pape ⁴ ,
Marius Lammers ³, Jörg Hermsdorf ³, Stefan Kaierle ³, Ludger Overmeyer ³ and Gerhard Poll ⁴

¹ Institut für Integrierte Produktion Hannover gGmbH, Hollerithallee 6, 30419 Hannover, Germany; stonis@iph-hannover.de

² Leibniz Universität Hannover, Institute of Materials Science, An der Universität 2, 30823 Garbsen, Germany; mildebrath@iw.uni-hannover.de (M.M.); faqiri@iw.uni-hannover.de (M.Y.F.); hassel@iw.uni-hannover.de (T.H.)

³ Laser Zentrum Hannover e.V., Hollerithallee 8, 30419 Hannover, Germany; l.budde@lzh.de (L.B.); a.barroi@lzh.de (A.B.); m.lammers@lzh.de (M.L.); j.hermsdorf@lzh.de (J.H.); s.kaierle@lzh.de (S.K.); l.overmeyer@lzh.de (L.O.)

⁴ Leibniz University Hannover, Institute of Machine Design and Tribology, An der Universität 1, 30823 Garbsen, Germany; coors@imkt.uni-hannover.de (T.C.); pape@imkt.uni-hannover.de (F.P.); poll@imkt.uni-hannover.de (G.P.)

* Correspondence: kruse@iph-hannover.de; Tel.: +49-511-27976-0

Received: 25 August 2020; Accepted: 2 October 2020; Published: 6 October 2020



Abstract: The service life of rolling contacts is dependent on many factors. The choice of materials in particular has a major influence on when, for example, a ball bearing may fail. Within an exemplary process chain for the production of hybrid high-performance components through tailored forming, hybrid solid components made of at least two different steel alloys are investigated. The aim is to create parts that have improved properties compared to monolithic parts of the same geometry. In order to achieve this, several materials are joined prior to a forming operation. In this work, hybrid shafts created by either plasma (PTA) or laser metal deposition (LMD-W) welding are formed via cross-wedge rolling (CWR) to investigate the resulting thickness of the material deposited in the area of the bearing seat. Additionally, finite element analysis (FEA) simulations of the CWR process are compared with experimental CWR results to validate the coating thickness estimation done via simulation. This allows for more accurate predictions of the cladding material geometry after CWR, and the desired welding seam geometry can be selected by calculating the cladding thickness via CWR simulation.

Keywords: tailored forming; cross-wedge rolling; welding; PTA; LMD-W; forming; rolling; coating

1. Introduction

Many technical applications place partly contradictory demands on the construction material used. For example, the parts may need to be lightweight, low-cost, and at the same time, increase performance. Material selection then becomes a multi-criteria decision problem in which factors such as production, costs, or environmental effects are considered [1–3]. The goals of the engineer may be conflicting [4]. The combination of multiple material types in a single component has the potential to achieve several goals at once, for example load bearing capacity can be varied through local adaptation

of material properties to reduce the overall amount of material required. Additive manufacturing, casting, and welding are currently used for this purpose [5–7].

In sheet metal forming, the use of welded sheet blanks, also known as tailored welded blanks, has been industrially established for over 20 years [8,9]. They are used in large quantities in the automotive industry for the production of body parts such as doors and side members [7]. However, the technology for this type of processing cannot directly be applied to a multi-material component with a three-dimensional geometry.

1.1. Tailored Forming Approach

Tailored forming involves deposition welding (see Section 2.1 and Section 2.2) and subsequent forming (see Section 2.3) to produce multi-material solid components [10]. An exemplary component of this process chain is shown in Figure 1 (left). Here, a multi-material shaft consisting of a cladding material (red) and a base material (blue) is shown. The deposition-welded part of the shaft (red) serves as a bearing race for a cylindrical roller bearing (CRB, yellow). Due to an external radial load on the CRB, high-contact normal stress exceeding 2 GPa [11,12] occurs in the contact between the rolling element and the shaft. According to the Hertz–Belyaev theory [13,14], the maximum equivalent stress occurs in a material volume below the stressed surface. When a loaded rolling element rolls over a point on the raceway surface, the maximum shear stress in the subsurface varies between 0 and τ_{\max} , see Figure 1, right. This cyclic loading of the material volume initiates and propagates fatigue cracks in the high-cycle regime ($\gg 10^6$ cycles), which is referred to as rolling contact fatigue (RCF) [15]. RCF eventually leads to material removal and, if a crack propagates to the surface and forms a chip/pitting, failure of the component. Lundberg and Palmgren [16] assumed the maximum orthogonal shear stress τ_O to be significant in causing fatigue failure. Other authors consider the von Mises–Hencky distortion energy theory [17] and the scalar von Mises stress to be better for predicting RCF failure, with the latter being directly proportional to the octahedral shear stress τ_{oct} . Figure 1, right, shows that the maximum shear stress occurs at depth z of approximately $0.5b$ to $0.8b$. Here, RCF occurs in a highly localized volume of stressed material, so a high-strength material is required there. The remaining part of the component can be made of a less solid material with higher ductility and lower price.

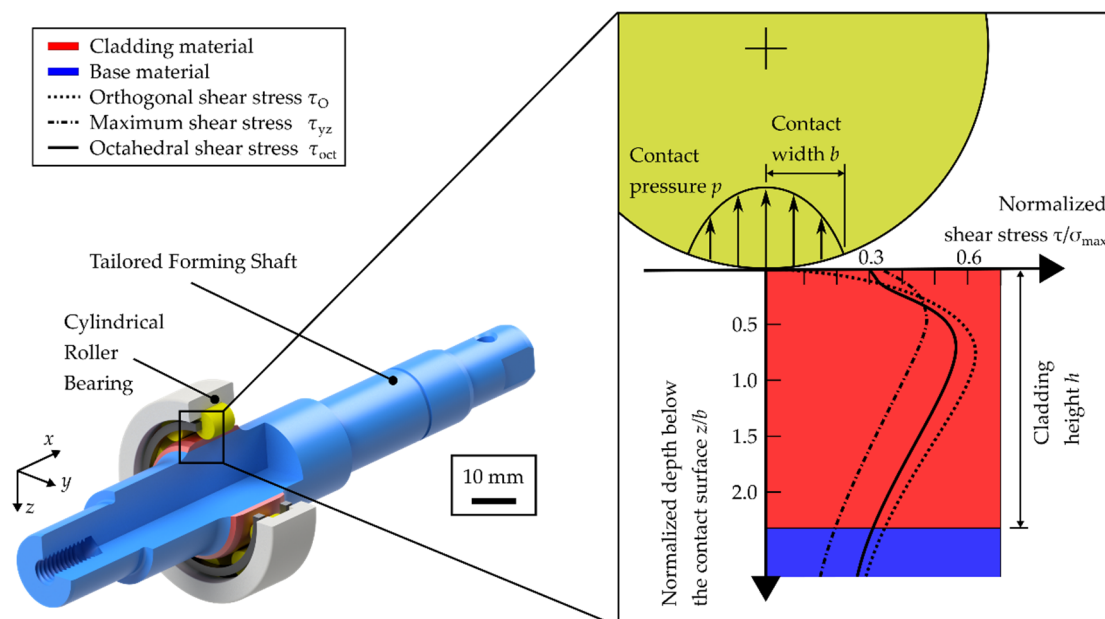


Figure 1. Partial section of tailored forming shaft with mounted cylindrical roller bearing (left) and loaded material volume (right).

1.2. Welding and Forming

Deposition welding is particularly suitable as a joining step, as it creates a substance-to-substance bond between the cladding material and base material. As already mentioned, the maximum stress zone of a roller bearing is under the contact surface. Surface hardening processes such as nitriding [18] do not reach the necessary layer thicknesses to withstand the expected loads. Through deposition welding, it is possible to produce a cladding layer, which can be adjusted to the applied forces and stresses by alloy design and thickness selection. It is also possible to deposit many kinds of metallic alloys, sometimes even those considered non-weldable because of their high carbon equivalent values (CEV). Further advantages of deposition welding are a low dilution rate and a high degree of automation [19].

The chosen deposition welding procedures are laser metal deposition welding with wire (laser metal deposition welding (LMD-W)) and plasma powder transferred arc welding (PTA). The welding processes were chosen for their different advantages. Laser metal deposition welding allows precise control of the seam geometry and produces low material dilution. PTA welding, on the other hand, allows significantly higher deposition rates but also introduces more heat into the components.

In laser metal-wire deposition welding, a wire is preheated using conductive heating and the laser radiation provides the energy necessary for melting the wire and the substrate material. The preheating of the wire reduces the required laser power, which leads to less heating of the substrate and thus to lower degrees of dilution between base material and applied material. Additional advantages of laser hot-wire processes are a better process stability and less sensitivity to tolerances in wire alignment. The low degrees of dilution ensure high quality of layers, so in most cases, the desired chemical or physical properties, such as corrosion resistance, wear resistance, and hardness, are achieved from the very first layer [20–22].

Plasma powder transferred arc welding is a thermal process for applying wear- and corrosion-resistant layers on surfaces of metallic materials. During the PTA welding process, a tungsten electrode creates a plasma arc with high energy density, which melts the surface of the base material. At the same time, the cladding material in powder form is streamed into the arc and molten. During solidification, a substance-to-substance bond between the cladding material and the base material is created. The whole welding process is performed with argon as the shielding gas.

In order to further enhance material- and process-related advantages, a subsequent forming of the joined semi-finished product is necessary.

It is possible to simulate forming processes in addition to welding processes with FEM. The prediction of the resulting heat flows is of particular importance. The mapping of heat flows allows an estimation of the heat-affected zones and the resulting residual stresses in the material. This is important, because it allows for prediction of component distortion. An example of how this can be achieved is given by Lostado Lorza et al. [23]. Due to the production process of the components used in this work, a simulation of the welding influence is not necessary. As Blohm et al. [24] showed, a hot forming process after a welding process could completely eliminate the heat effects of welding on the steel structure. The reason for this is the complete re-austenitization of the microstructure with subsequent microstructure formation, which neutralizes previous residual stresses. As shown in Figure 2, this microstructure transformation can also be observed in the samples of this work. Figure 2a shows the microstructure of the base material C22.8 after welding. A classical Widmanstätten microstructure of long ferrite needles can be seen, and the impact of the heat from welding is obvious. The 100Cr6 is solidified in a pearlitic structure and is located in the darker region in the upper part of the picture. After cross-wedge rolling (CWR), the microstructure in the base material and in the coating material is much finer-grained than after welding and corresponds to a typical microstructure from forming (Figure 2b). In both microstructure states, a defined orientation of the grains or inhomogeneity cannot be identified, so for the simulation of the forming process, isotropic forming properties are assumed.

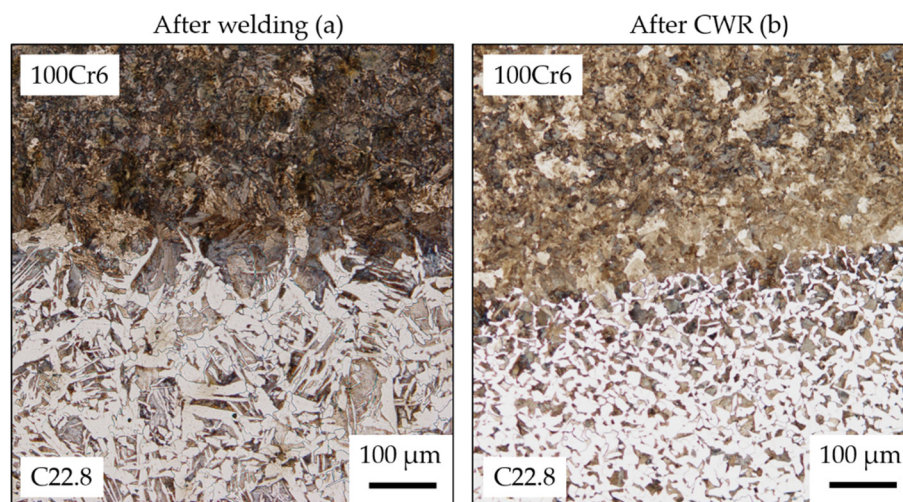


Figure 2. Microstructure of the joining zone after welding (a) and after cross-wedge rolling (CWR) (b).

1.3. Bearing Fatigue Life of Tailored Forming Machine Elements

Previous investigations [25,26] have shown that the performance of tailored forming machine elements, in particular their fatigue life, is dependent on the layer height of the cladding material. The cladding height h is defined as the radial distance between the rolling element/shaft contact point at one end, and the cladding layer/base material interface at the other, see Figure 1 (right).

Figure 3 shows the calculated bearing fatigue life for different radial loadings and cladding heights with test data for a monolithic specimen as reference [26]. Here, fatigue-life simulations were carried out for a radial loading on the tested CRB of $F_{\text{rad}} = 2$ kN with a resulting Hertzian contact pressure of $p_{\text{max}} = 1.8$ GPa. The calculated bearing life L_{50} , where 50% of the specimens are expected to have failed, is $L_{50} = 23.5 \times 10^6$ revolutions. This is within an error margin of 16% of the bearing fatigue life from the experimental studies. The basic trends of the calculated probability of survival are represented by the experimental values L_{10} and L_{63} . A too-thin cladding layer reduces fatigue life of multi-material machine elements by a factor of 3. With a cladding height of $h > 0.5$ mm the difference in fatigue life compared to monolithic parts is within a 15% margin. These preliminary results show that a minimum cladding height in dependence of the load is necessary to achieve the same fatigue life as a monolithic component.

The approach for hybrid roller bearings is particularly interesting for large scales. Large-diameter bearings are currently manufactured from classic forging materials such as 42CrMo4, which are not specifically designed for roller bearing applications. By coating the running surfaces with a small amount of a high-performance material, it would be possible to increase the service life enormously or to use the bearings in much more corrosive environments.

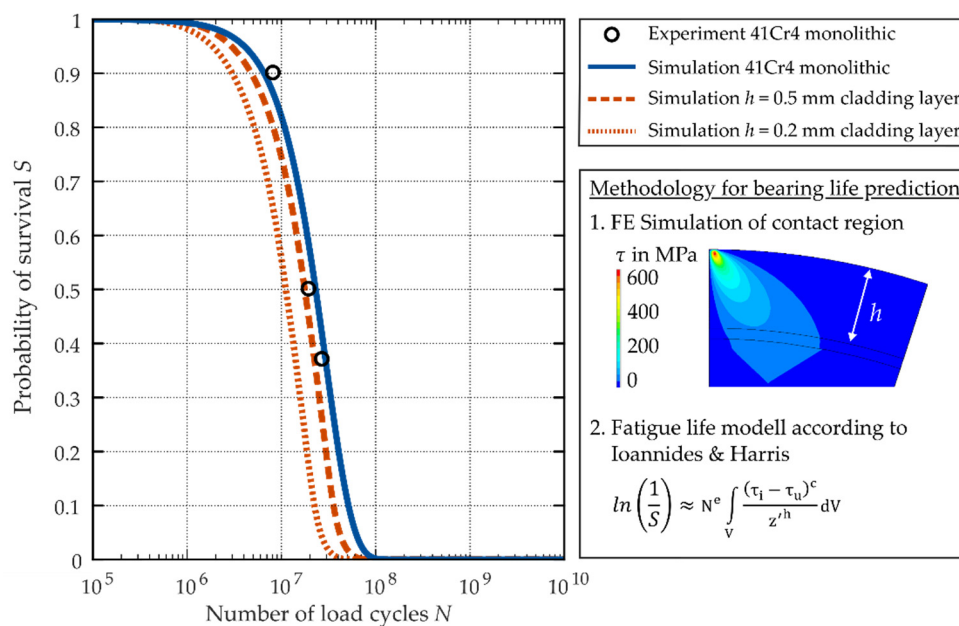


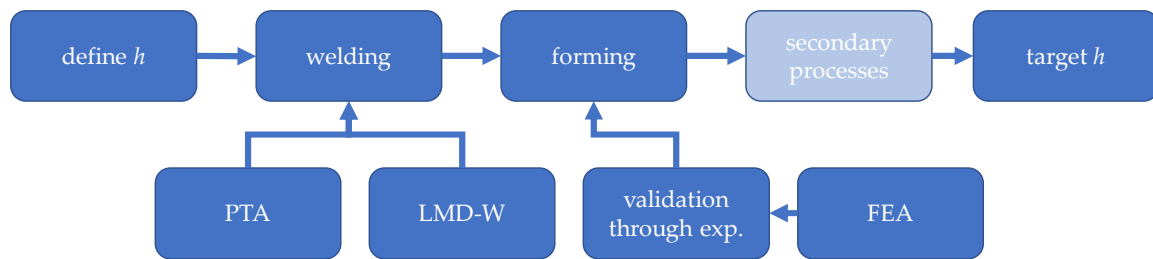
Figure 3. Bearing fatigue-life simulation for different cladding layer thicknesses.

2. Materials and Methods

For the reasons given in the previous chapter, the production process for manufacturing tailored forming machine elements must meet the following conditions to be implementable in industrial applications:

- Depending on the application, even a small amount of high-performance material may be sufficient to produce a multi-material component with a performance comparable to that of conventional manufacturing processes. However, the cladding layer in the region subject to rolling contact loading must not be too thin.
- The process must have an economically viable application rate and quality. This requires precise knowledge of the application and its loads.
- It must be possible to set the layer height as the decisive target value for production within narrow limits.

The aim of this paper therefore is to achieve a precise adjustment of the cladding thickness h by controlling the production process, see Figure 4. For this purpose, first, two different joining processes—laser metal deposition welding and plasma-transferred arc welding—are presented in Sections 2.1 and 2.2, and the characteristics that particularly influence cladding thickness are empirically examined using welding test rigs. Subsequently, cross-wedge rolling as a forming process is described in Section 2.3, and the decisive variables that influence layer height are worked out. Extensive numerical analyses are performed, which are validated by experimental investigations on a test rig. The purpose of these cross-wedge rolling experiments is to determine the input geometry with regard to width and height of the cladding layer in advance. In this way, the fatigue-life requirements for the application can be reconciled with the target parameters for deposition welding.



PTA: Plasma Powder Transferred Arc Welding
 LMD-W: Laser Metal Deposition Welding with Wire
 FEA: Finite Element Analysis
 h : cladding thickness of welded material
 exp.: Experimental investigations

Figure 4. Methods for defining cladding material distribution.

Two different cladding materials are used for the investigation. The martensitic chrome silica steel X45CrSi9-3 is used as cladding material for the laser metal deposition by wire process. The cladding material for the PTA process consists of the roller bearing steel 100Cr6, which has a CEV > 1 and is therefore difficult to weld [27]. The material has a high resistance against cyclic loading. The 100Cr6 powder is filtered with a sieving unit. Only powder consisting of metal grains with a diameter between 63 μm and 200 μm is used for the welding [28]. This corresponds to the current industrial standard for additional materials in powder form that are used for welding. The basic material of the shafts consists of the unalloyed and heat-resistant steel C22.8, which is mainly used in valve construction and is considered to be easily to weld. The chemical composition of base material and cladding material are shown in Table 1.

Table 1. Chemical composition in wt.% of C22.8, X45CrSi9-3, and 100Cr6.

Material \ Element	C	Si	Mn	P	S	Cr	Ni
C22.8	0.17–0.24	<0.40	0.40–0.70	<0.045	<0.045	<0.40	-
X45CrSi9-3	0.4–0.5	2.7–3.3	≤ 0.6	≤ 0.004	≤ 0.03	8.0–10.0	≤ 0.5
100Cr6	0.93–1.05	0.15–0.35	0.25–0.45	≤ 0.025	≤ 0.015	1.35–1.60	-

2.1. Laser Metal Deposition Welding with Wire

Hybrid semi-finished products are manufactured by deposition welding of the martensitic chrome silica steel X45CrSi9-3 onto a base cylinder made of the unalloyed steel C22.8. A coaxial laser hot-wire welding head is used to produce the hybrid components. Compared to lateral wire feeding, coaxial wire feeding has the advantage that the process is independent of the welding direction and is therefore suitable for the manufacturing of complex components [29,30].

Base cylinders with a diameter of 27 mm and 29 mm are used as substrate. The substrate is sandblasted and then cleaned with ethanol and kept at room temperature without any preheating.

For manufacturing of the hybrid semi-finished products, the base cylinder is placed in a rotary axis, which can be moved in the X–Y plane. By superimposing the rotational movement of the base cylinder and the movement of the rotational axis in the x-direction, spiral seams are applied to the base cylinder. The processing head does not move during welding. The welded layer is positioned in the middle of the base cylinder (see Figure 5).

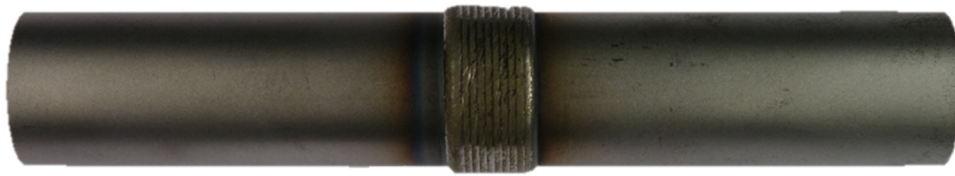


Figure 5. Shaft with cladding applied by laser metal deposition with wire.

Hybrid semi-finished products with various geometries are produced to validate the simulation of the layer distribution during CWR. Cladding layers consisting of 6 or 11 adjacent seams with a width of 8 or 15 mm, respectively, are applied to these using the before-mentioned setup. The claddings are applied in one or two layers, whereby the two layers were welded unidirectionally, with a short break of 90–120 s between layers.

An overview of the welding parameters is shown in Table 2.

Table 2. Welding parameters for laser metal deposition with wire.

Parameter	LMD-W ¹
Welding speed	1200 mm/min
Current	110 A
Wire feed rate	2.8 m/min
Laser power	2.3 kW
Shielding gas flow	8 L/min
Wire diameter	1.0 mm

¹ Laser Metal Deposition Welding with Wire.

Examples of the seam geometry after deposition welding are shown in Figure 6. The seam height is approx. 1.2 mm for single-layer deposition and approx. 2.4 mm for double-layer deposition.

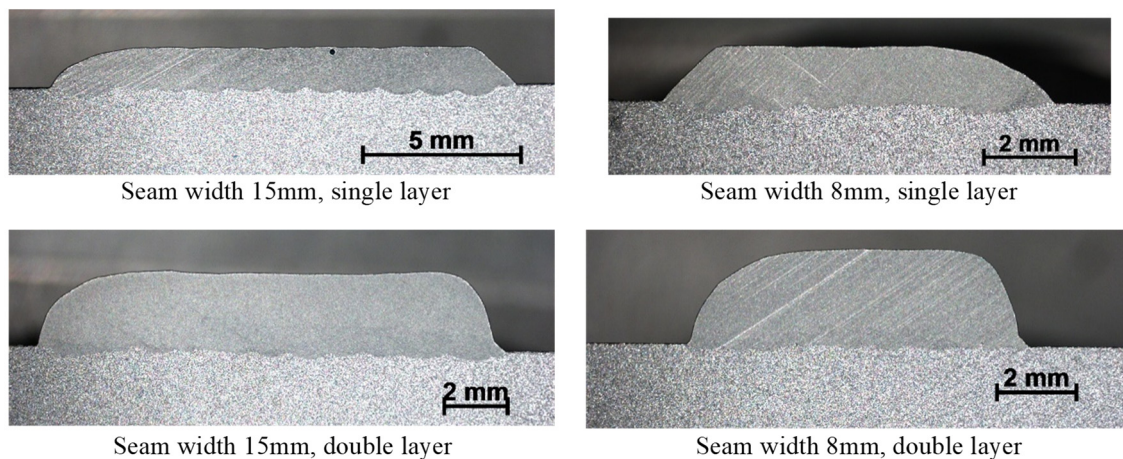


Figure 6. Examples of the seam geometry after deposition welding.

For each set of parameters, one shaft after welding and one shaft after CWR is cut, and the layer distributions are evaluated. The values for characteristics of the welded layer are used as input variable data for the simulation.

2.2. Plasma Powder Transferred Arc Welding

The PTA welding process is carried out by a six-axis REIS RV industrial robot (KUKA AG, Augsburg, Germany), where two additional axes are realized by a turn and tilt table. The welding torch is the Kennametal Stellite HPM 302 (Kennametal GmbH, Rosbach, Germany), which is water-cooled.

First, the bar blanks are turned and cut to size. The finished components have a length of 150 mm and a diameter of 27 mm. Prior to the welding process, the components are cleaned with acetone to get clean surfaces. The components are welded at room temperature. For the welding process, the shaft is fixed in the additional axis and aligned parallel to the ground. The welding head is in a horizontal welding position aligned with the shaft. During the welding process, the welding head only moves with a defined pendulum movement in the y-direction, while the shaft rotates 6 times around its own axis. The result is a spiral weld seam, which is 30 mm long in total (see Figure 7). The weld seam is welded a little longer than required, because the beginning and the end of the seam cannot be welded in an optimum way for technical reasons.



Figure 7. Welding seam after cladding by PTA.

To achieve an even application layer, it is important that the weld pool has enough time to solidify. Because of the small diameter and the rotation of the shaft, there is a risk that the weld pool does not cool down in time and drops to the ground due to gravity. Therefore, the torch is moved slightly off the center-point, which increases the arc length and gives the weld pool more time to cool down. In order to apply the weld seam as homogeneously as possible and to avoid pores, the welding torch oscillates over a short distance of 4.5 mm in the welding direction with a frequency of 1 Hz. This slightly increases the dynamics of the weld pool and allows degassing of the melt, which reduces the chance of pore formation. The whole welding process takes about 5 min, and the shaft reaches 700 °C. In order to counteract a strong heating of the cladding and base material, the temperatures are dynamically adjusted during the welding process. At the beginning, a current of 120 A is selected to generate a fast heating of the shaft. Further in the process, the current is gradually reduced in order to keep the dilution low and as constant as possible (see Figure 8). An overview of the general welding parameters is shown in Table 3.

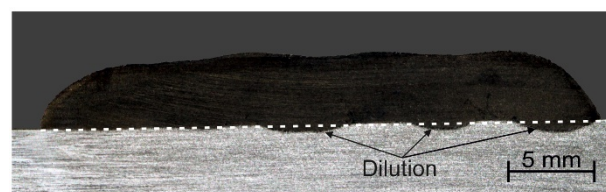


Figure 8. Dilution during the welding process.

Table 3. Welding parameters for plasma powder transferred arc welding.

Parameter	Value
Shielding gas flow	10 L/min
Plasma gas flow	1.5 L/min
Transport gas flow	6 L/min
Welding speed	0.06 m/min
Length of the welding seam	30 mm
Current	120–100 A
Voltage	27–25 V (depends on current)
Powder material	100Cr6
Grid size of powder particles	0.06–0.2 mm
Deposition rate	0.9 kg/h

2.3. Cross-Wedge Rolling

Cross-wedge rolling is an efficient way to distribute masses on work pieces as a preform operation prior to forging or milling [31]. During the CWR process, material is axially shifted by wedge geometries on the tool surface (see Figure 9). Depending on the wedge geometry, reductions in diameters up to 90% can be achieved with high reproducibility [31]. CWR is one of the forming processes investigated within the tailored forming process chain, next to die forging and impact extrusion. The forming parameters of the CWR process have impact on the quality of the hybrid parts produced within the process chain, especially with regard to machining. Depending on the forming temperature and heating strategy, the forming velocities and tool spacing can have an influence on the quality of the rolled part [32,33]. Figure 9 shows the typical process of cross-wedge rolling, which is being investigated experimentally and via simulation.

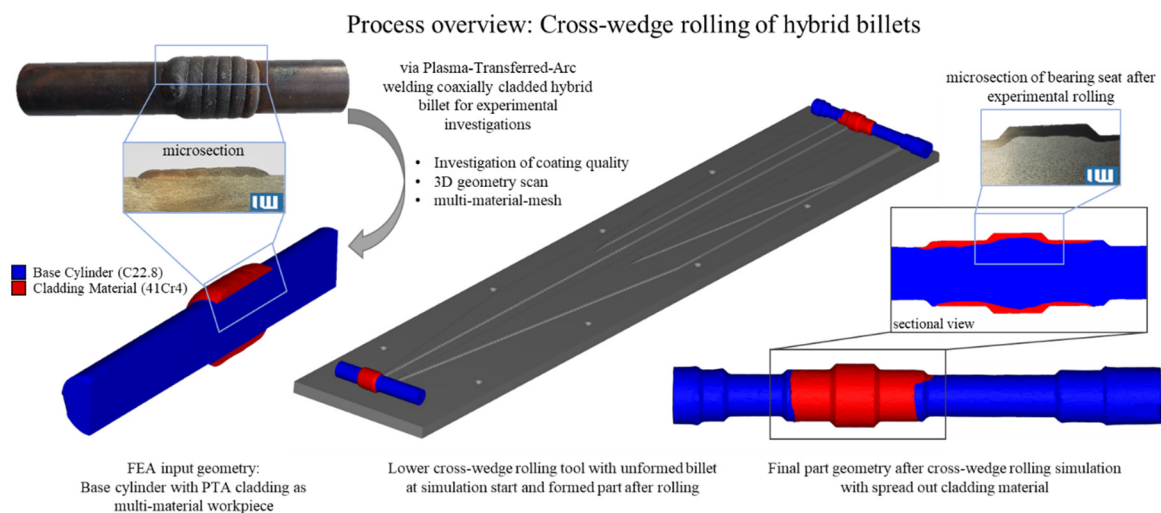


Figure 9. Process overview of cross-wedge rolling of hybrid work pieces.

In this paper, the influence of the CWR process on the forming behavior of differently welded semi-finished workpieces is investigated with regard to its predictability via simulations and its potential influence on the service lifetime of hybrid parts. For this, differently shaped work pieces were welded, as shown in Section 2.1 and Figure 6. Out of the various types of workpieces, several were formed by CWR. At least three of the work pieces were cut in half after CWR, so that the material distribution of the cladding material could be examined. The CWR process was the same as that shown in Figure 9. The other halves of the formed work pieces then continued along the process chain until the final step of the research was reached: service life investigations.

2.3.1. Cross-Wedge Rolling Simulation

Before any experimental investigations of cross-wedge rolling were conducted, the process was first simulated, to save resources and time. As mentioned before, finite element analysis (FEA) can accurately depict the CWR process [33,34]. The simulations were calculated within the commercial FEA software Forge NxT 3.0, developed by TRANSVALOR S.A. (CS 40237 Biot, 06904 Sophia Antipolis cedex, France). No custom subroutines were used. The simulations were set up within the graphical user interface of the software. No modifications to the software were made.

The tool geometries within the simulation are based on the Computer Aided Design (CAD) files of the tools that are used for the experimental trials. The advantage of the symmetry of parts in the area of the bearing seat was used to reduce calculation time (Figure 10).

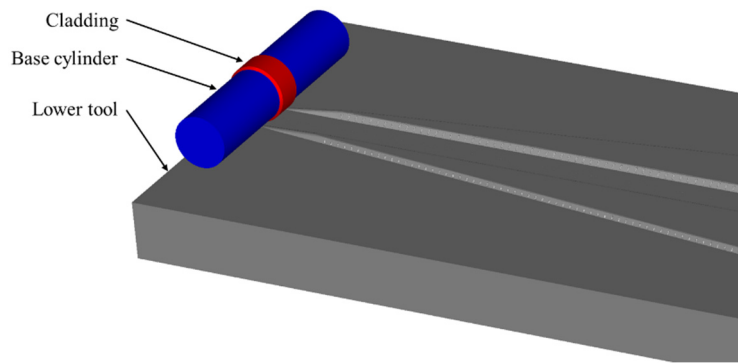


Figure 10. CAD model of hybrid work piece and lower cross-wedge rolling tool as FEA input.

Only the first 1.5 s of the 11-s forming process were investigated, because that is when the bearing seat geometry is formed. After that, the rest of the part is formed. Figure 11 shows the final simulation step used to investigate the cladding distribution after forming the bearing seat region. Figure 12 shows the process at different stages during simulation. The kinematics are analogous to the forming of the area in the experimental trials.

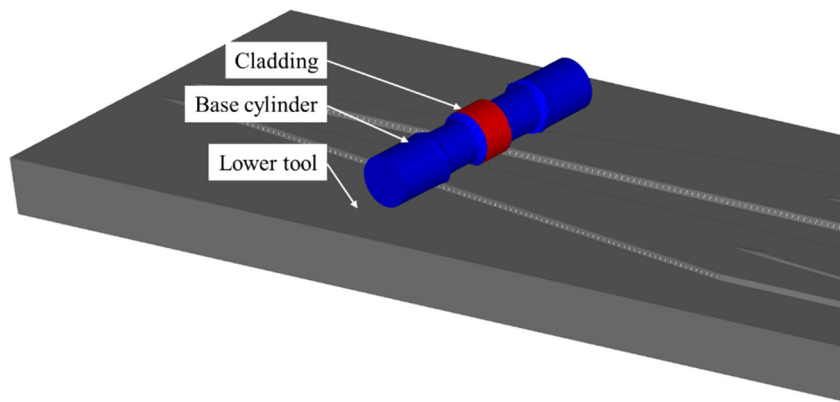


Figure 11. Simulation result of hybrid work piece cross-wedge rolling tool after 1.5 s process time.

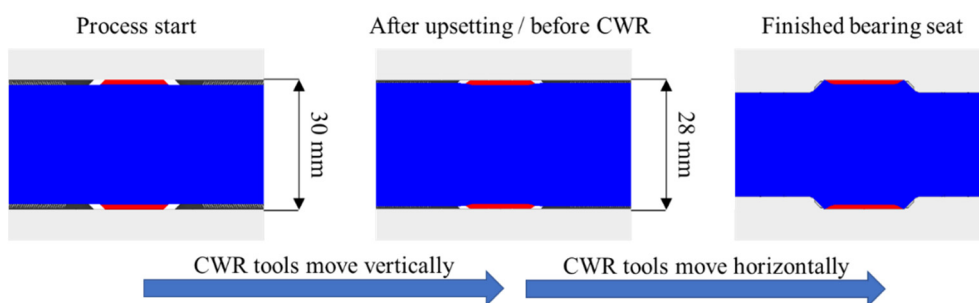


Figure 12. Cross-wedge rolling process at different time steps, where the base cylinder is in blue and the cladding in red.

To further improve calculation duration, different mesh sizes of tetrahedral elements were used within each billet. The mesh sizes were analytically investigated within a mesh sensitivity analysis in previous work. Nonlinear shape with coupled thermal-mechanical functions were used. Especially for hybrid parts, choosing the optimal mesh sizes improves calculation times drastically while still giving significant results. In Forge NxT, contact is considered using a velocity field penalization method, which allows for a slight penetration of the part into the die. This is the only method/algorithm available by default [35].

The quality of a volume mesh generated in Forge NxT is measured using the surface and the volume shape factor. “The surface shape factor is the simplest criteria and should be investigated first. It indicates whether the element is close to (=1) or far away from ($\ll 1$) the ideal equiangular triangle shape. It can also detect degenerate (<0), flat (=0), or quasi-flat ($\rightarrow 0$) elements.” [35]

The volume shape factor “determines whether the elements are close to (=1) or far away from ($\ll 1$) the ideal equiangular tetrahedron shape. It can also detect degenerate (<0), zero volume (=0), or quasi-flat ($\rightarrow 0$) elements.” [35]

The remeshing algorithm is triggered if the quality is below 0.4. The quality is computed as a ratio between the surface and the square perimeter of an element [35]. The volume and surface shape factor were above 0.75 (0.4 is considered the recommended minimum [35]).

The distortion value was calculated as approximately 0.82. In order to measure element distortion while eliminating the scale factor between parent and actual element referential, a “normalized” value of the Jacobian, defined as the product of the original Jacobian and a correction term K , was computed. This is automatically done by Forge and can be displayed to the user [35].

The bearing seat area was meshed with a mesh size of 1 mm, and the rest of the work piece was discretized with a mesh size of 3 mm. For the initial material distribution, the multi-material-set feature of Forge NxT 3.0 was used. Early simulations within subproject B1 (before Forge NxT 3.0 was released) were realized by modeling the base cylinder and the cladding material as separate objects within the simulation, which were then linked by bilateral sticking. The heat transfer between cladding and base cylinder was not satisfactory [32]. As a result of close communication with Transvalor with regard to the needs of simulation for hybrid work pieces, the multi-material-set feature was improved in Forge NxT 3.0. Therefore, it is now possible to load one geometry as work piece and define the segments of the work piece that are supposed to be made of a different material. This results in one mesh in which certain elements can be of a different material from the others. This approach also improves the accuracy of remeshing, which is indispensable, due to the high degrees of deformation. The flow curves for the material C22.8 were created using a Gleeble 3800-GTC (Dynamic Systems Inc., Poestenkill, New York, USA) and a DIL 805A/D+T dilatometer (TA Instruments, New Castle, USA). The cladding material was taken from the Forge NxT Database and was fitted for the Hensel and Spittel approach. This model describes the forming behavior of the material in dependence of the temperature T , the effective strain, the flow behavior by parameter ϵ , and the strain rate $d\epsilon/dt$. Within Forge NxT, the Hensel and Spittel equation is simplified [35,36], resulting in a viscoplastic material model. The flow curves and parameters of several materials were input in Forge NxT. The initial work piece temperature was set to 1250 °C and the tool surface temperature to 250 °C. The tool velocity for rolling was set to 250 mm/s for each tool. The translational movement of the tools was generated by the hydraulic press preset. Before rolling, the work piece is slightly upset with vertical force. This is realized by the upper tool moving towards the lower tool for 1 s, reducing the spacing of the tools from 32 to 28 mm. The heat transfer between tools and work piece was set to the preset “steel hot medium”, resulting in an alpha value of 10^4 W/m²K. The thermal effusivity of the tools was set to 11.76 kJ/m²·K·s^{0.5}. The ambient air temperature was set to a constant temperature of 50 °C. The chosen preset “steel hot medium” and the heat-exchange algorithm within Forge NxT take conduction, convection and radiation between the tools, work piece, and ambient air into account. The friction between work piece and tools were set to the preset “very high Tresca”, resulting in a value $m = 0.8$, which proved to be a good approximation of friction for hybrid CWR processes [32]. As default, thermal expansion calculation is not enabled for material flow simulations in Forge NxT. Additionally, as default, rigid dies are used to simulate a CWR process. To assure the accuracy of the simulation model used, simulations comparing these influences were conducted and the cladding thickness for each set of parameters was measured within Forge NxT (see Figure 13).

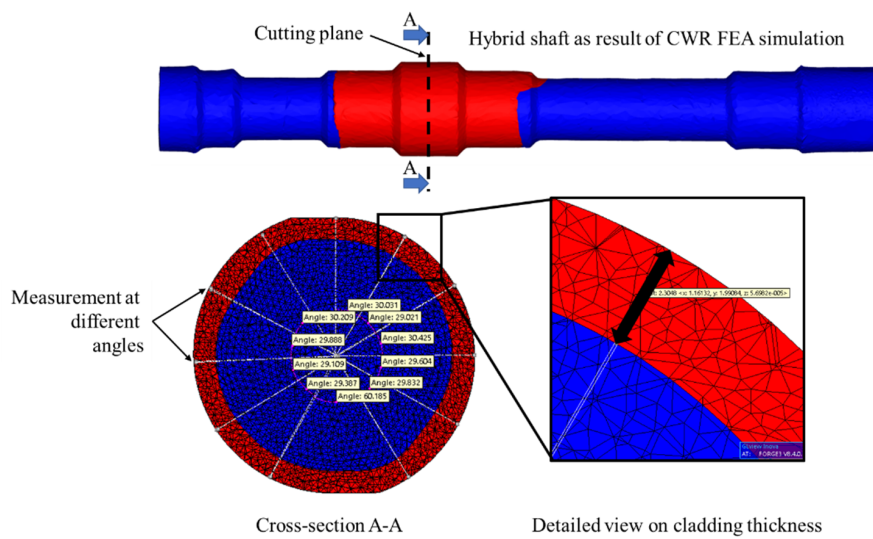


Figure 13. Measurement of the cladding thickness in the center of the bearing seat.

For this purpose, three different simulations setups (Table 4) were calculated up to the point where the cross-section of the bearing seat is nearly completely shaped. The results were compared. As Table 5 shows, the deviations between the results of the different FEA setups is small (deviation of <math>< 2.5\% = 0.058\text{ mm}</math> for the avg. cladding thickness), keeping in mind that the average mesh size in this cross-section area is approximately 1 mm. Therefore, the accuracy with the default settings is sufficient to predict the material flow behavior under justifiable expenditure of calculation time (Table 4). For setup #3, the calculation took more than 160 h, which is too long when simulating an array of variations.

Table 4. Comparison matrix for FEA calculation time of cross-wedge rolling of work piece.

Case ID	Thermal Expansion Calculation ¹	Tool Behavior	Thermal Expansion due to Initial Heating ¹	Estimated Normalized Calculation Time
#1	No	rigid	No	100%
#2	Yes	rigid	Yes	182%
#3	Yes	deformable	Yes	449%

¹ of work piece.

Table 5. Deviation comparison of different FEA setup results of the cross-wedge rolling process.

Simulation Result	Setup	Cross Section Surface of:		Max. Coating Thickness	Min. Coating Thickness	Avg. Coating Thickness
		Cladding	Base Cylinder			
	#1: No thermal expansion; Rigid tools	644.082 mm ²	452.646 mm ²	2.263 mm	2.854 mm	2.439 mm
	#2: Thermal expansion; Rigid tools	644.912 mm ²	455.057 mm ²	2.101 mm	2.830 mm	2.426 mm
	Δ to Setup #1	0.10%	0.50%	7.20%	0.80%	0.50%
	#3: Thermal expansion; Deformable tools	643.981 mm ²	430.330 mm ²	2.131 mm	2.872 mm	2.381 mm
	Δ to Setup #1	0.00%	5.20%	6.20%	0.60%	2.40%

Due to the little impact of the thermal expansion and tool elasticity, the simulations were set up with rigid dies and no thermal expansion calculation. The parameters used within the simulation are shown in Table 6.

Table 6. Simulation parameters used within the model of the hybrid cross-wedge rolling process.

Material	Work Piece Geometry	Tool Velocity	Work Piece Temperature
Base cylinder: C22.8 Cladding: X45CrSi9-3 or 100Cr6	Ø 27 or 29 mm 8 or 15 mm width; 1.2; 2.4; or 2.5 mm height	240 mm/s	1250 °C

Besides the work piece geometry, all simulation parameters remained the same for all investigations. Four types of cladding geometries were used for the material X45CrSi9-3 and combined with two different base cylinder diameters (27 and 29 mm), which results in eight work piece variants. For 100Cr6, three cladding geometries were used and a 27 mm diameter due to limited availability of base cylinders in the chosen dimensions. After the hybrid semi-finished work pieces were welded, they were cooled down at ambient air conditions. The cooled-down work pieces were cut in half, and the different cladding thicknesses were measured (Figure 6). The geometry of all 100Cr6 parts was created by milling similar welded work pieces (Figures 7 and 14) to three different geometries: 10, 15, and 20 mm seam width and 2.5 mm seam height (Figure 14). This was done due to the less accurate layer application of PTA welding compared to the hot-wire deposition welding. This was the most reproducible way to immediately get similar cladding geometries.



Figure 14. Work piece 100Cr6/C22.8 milled to 27 mm diameter and 10 mm cladding material seam.

The average thickness of each cladding layer and its width were measured and input for the simplified geometry of the simulation. The various adapted geometries are shown in Figures 15 and 16.

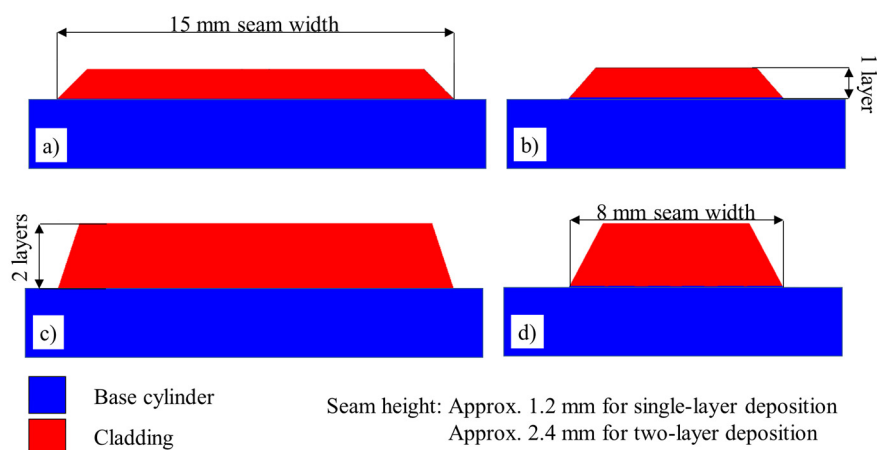


Figure 15. CAD model of different cladding (red) distributions on base cylinder (blue) for X45CrSi9-3, (a) 1 layer at 15 mm seam width (b) 1 layer at 8 mm seam width (c) 2 layers at 15 mm seam width (d) 2 layers at 8 mm seam width.

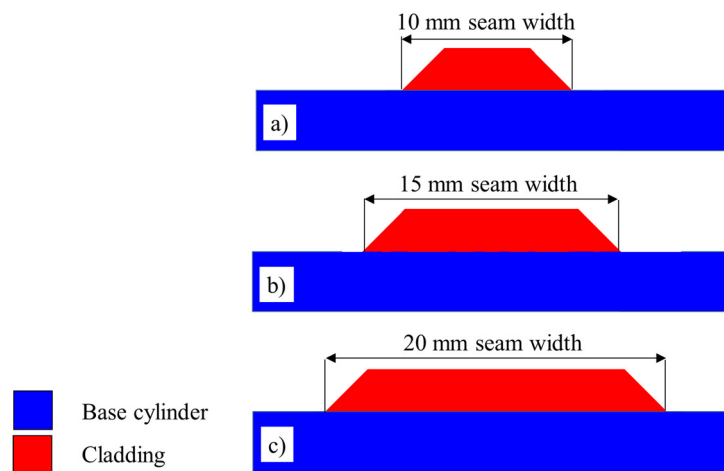


Figure 16. CAD model of different cladding (red) distributions on base cylinder (blue) for 100Cr6, (a) 10 mm seam width (b) 15 mm seam width (c) 20 mm seam width.

After the simulations were calculated, the material distribution was analyzed. The results of the simulation will be discussed in Section 3.

2.3.2. Cross-Wedge Rolling Experiment

For experimental investigations, the CWR module (a self-built test stand) of the Institut für Integrierte Produktion Hannover gGmbH (IPH) was used (see Figure 17). The module consists of a machine frame in which two sleds can glide by translatory motion. The sleds have mounting holes for the CWR tools. The translational (horizontal) movement of the sleds is created by hydraulic cylinders, providing each sled with up to 125 kN of force. The vertical force, which is necessary to ensure constant spacing between the tools, regardless of the forming forces, is generated by the hydraulic press into which the module is mounted. The 6,300 kN press (manufactured by NEFF) is set to 50 kN of closing force. The minimum spacing is ensured by spacing discs with standardized heights that function as a vertical end-stop.

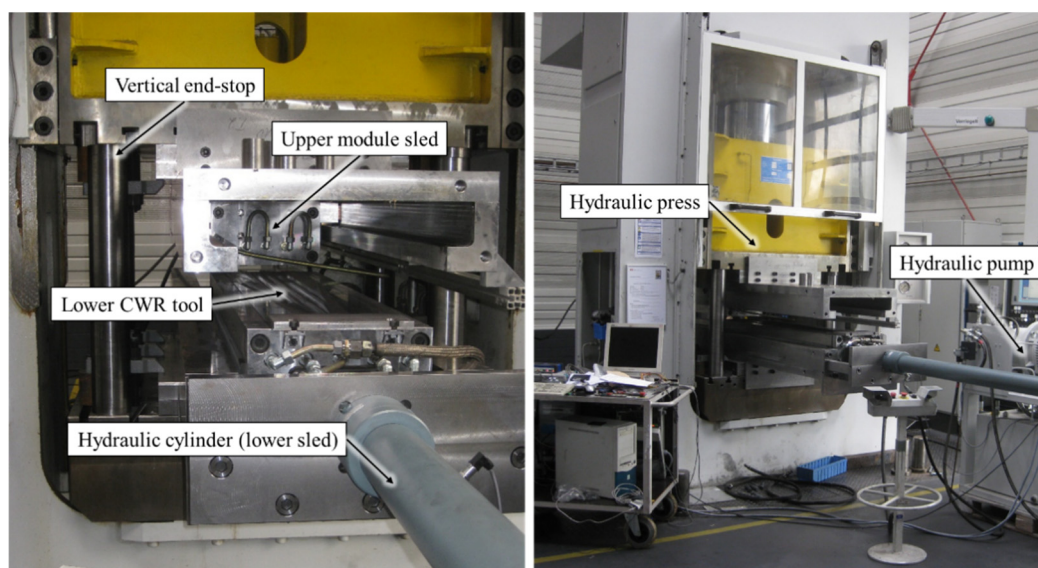


Figure 17. Cross-wedge rolling test stand at the Institut für Integrierte Produktion Hannover.

Prior to CWR, the parts need to be heated. This can be done using either the furnace or the IPH induction heating unit (manufactured by EMA-TEC GmbH). The advantage of the furnace is the

close to perfectly homogenous heating of the part, whereas induction heating creates slight gradients of temperature within the work piece. Nevertheless, the short amount of heating time (60 s) used compared to the furnace (at least 40 min) results in less scale on, and less surface decarburization in the surface of, the work piece. With extensive heating, too little carbon may remain to harden the surface of the bearing seat after rolling and milling. Therefore, the work pieces were heated by induction heating for this research. The work pieces were heated for 60 s, resulting in approx. 0.4 kWh of energy induction into the work piece, which led to a peak temperature of 1300 °C, before the 20 s for transport into the CWR module. After transport, the work piece retained a temperature around 1250 °C. The tools were heated by heating cartridges to a temperature of 200 °C. The bottom of each tool was isolated with a polymer plate made of AS600M to reduce temperature leakage. Figure 18a shows a variety of hybrid work pieces with different amounts of the cladding material shown in Figure 6.



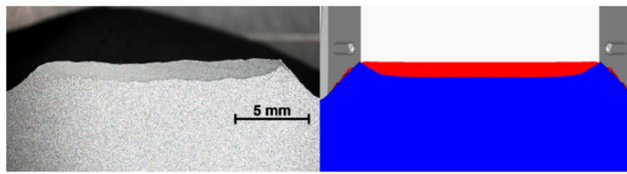
Figure 18. (a) Work pieces with different amounts of cladding; (b) (cold) work piece in starting position.

The work pieces were placed with their center aligned to the center of the bearing seat forming wedges. A mechanical end-stop ensured correct positioning (Figure 18b). After positioning, the upper tool was lowered onto the end-stops with 50 kN of force, resulting in a defined rolling gap of 28 mm. As soon as the desired gap width was reached, the hydraulic cylinders of the tool sleds were moved to start the rolling process, which took about 9 s. After rolling, the work pieces were taken out of the CWR module and placed onto a steel tray to slowly cool in air with free convection to prevent hardening and distortion. When cooled down, the work pieces were cut in half to examine the material distribution and to check for defects, as shown in Figure 9.

3. Results

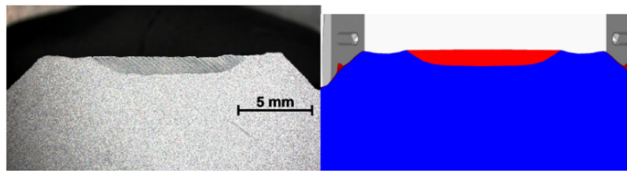
The cladding distribution and thickness in the simulation can be compared to experimental results for every parameter combination. From now on, the parameter combinations will be given as a string based on the diameter of the base cylinder, the cladding width and number of layers (e.g., 27_15_1). The simulation pictures for X45CrSi9-3 were taken at 1.25 s of process time. The pictures of the experiment were taken after completion of the CWR process and subsequent splitting in half.

As shown in Figures 19–26, the results of the simulations are similar to the experimental findings. Especially for the parameter combinations with 27 mm base cylinder diameter and one cladding layer, the shape and the measurements are very similar (Figures 19–21; Figure 25). The deviations are within the margin of error. The parameter combination 27_15_1 (Figure 19) shows a deviation of 0.45% in cladding width and 3.47% in cladding height, resulting in only 0.04 mm difference in cladding height between simulation and experiment, which is almost indistinguishable.



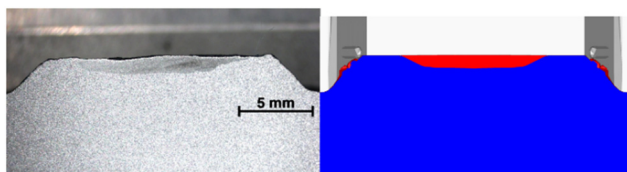
X45CrSi9-3	Experiment	Simulation	Δ
Cladding width in mm	17.6	17.52	0.45%
Cladding height in mm	1.11	1.15	3.47%

Figure 19. Comparison experiment/simulation; 27 mm base cylinder, 15 mm cladding width, 1 layer.



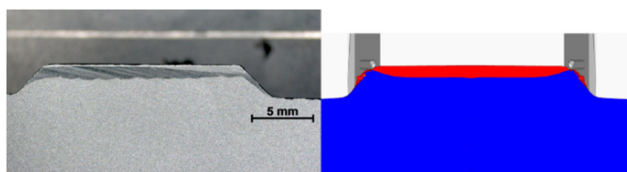
X45CrSi9-3	Experiment	Simulation	Δ
Cladding width in mm	10.59	11.44	7.43%
Cladding height in mm	1.14	1.21	5.79%

Figure 20. Comparison experiment/simulation; 27 mm base cylinder, 8 mm cladding width, 1 layer.



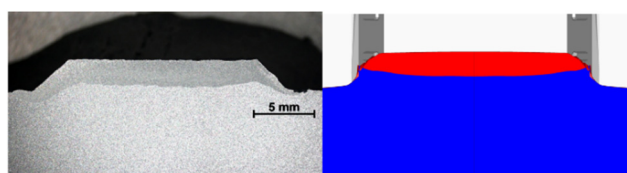
X45CrSi9-3	Experiment	Simulation	Δ
Cladding width in mm	11.92	12.02	0.83%
Cladding height in mm	1.17	1.07	9.35%

Figure 21. Comparison experiment/simulation; 29 mm base cylinder, 8 mm cladding width, 1 layer.



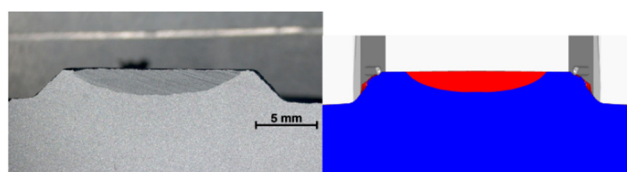
X45CrSi9-3	Experiment	Simulation	Δ
Cladding width in mm	20.16	19.1	5.55%
Cladding height in mm	1.25	1.13	10.62%

Figure 22. Comparison experiment/simulation; 29 mm base cylinder, 15 mm cladding width, 1 layer.



X45CrSi9-3	Experiment	Simulation	Δ
Cladding width in mm	23.89	21.7	10.09%
Cladding height in mm	2.06	2.31	10.82%

Figure 23. Comparison: experiment/simulation; 29 mm base cylinder, 15 mm cladding width, 2 layers.



X45CrSi9-3	Experiment	Simulation	Δ
Cladding width in mm	13.72	13.9	1.29%
Cladding height in mm	2.06	1.98	4.04%

Figure 24. Comparison experiment/simulation; 29 mm base cylinder, 8 mm cladding width, 2 layers.

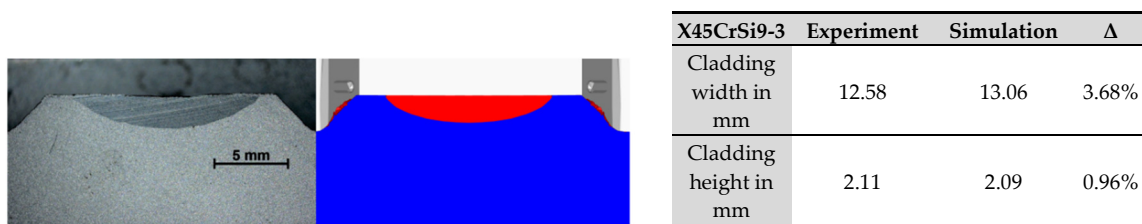


Figure 25. Comparison experiment/simulation; 27 mm base cylinder, 8 mm cladding width, 2 layers.

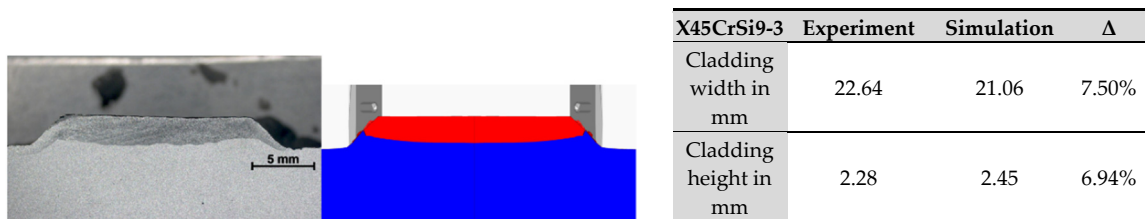


Figure 26. Comparison experiment/simulation; 27 mm base cylinder, 15 mm cladding width, 2 layers.

For the 100Cr6 work pieces (Figures 27–29, simulation picture taken at 2.0 s process time), the deviations between simulation and experiment decrease with increasing amount of cladding material. The overall shape of the cladding after rolling is comparable to the results of the simulation and, in the best case (Figure 29), below 3% deviation. Comparing the 15 and 20 mm cladding widths, it can be shown that the increase in cladding height is marginal. The additional cladding material just flows out of the bearing seat area without any use in future application. Which height will be sufficient for 100Cr6 hybrid shafts will be investigated in future research.

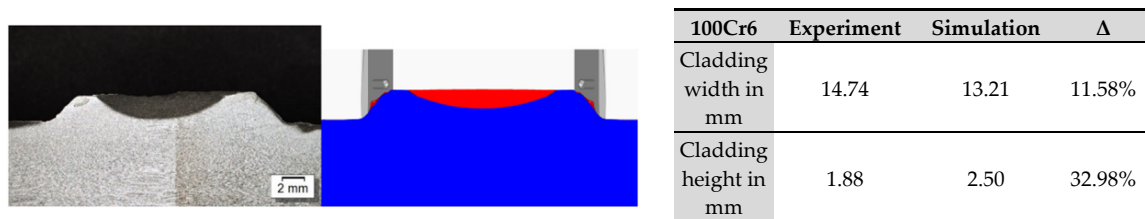


Figure 27. Comparison experiment/simulation 100Cr6, 27 mm base cylinder, 10 mm cladding width.



Figure 28. Comparison experiment/simulation 100Cr6, 27 mm base cylinder, 15 mm cladding width.

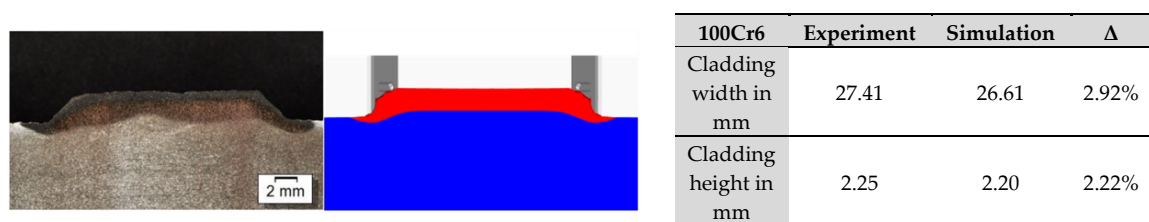


Figure 29. Comparison experiment/simulation 100Cr6, 27 mm base cylinder, 20 mm cladding width.

The parameter combinations with 29 mm base cylinder bear more cladding after welding, since the diameter is increased, while the same initial layer height is kept. Therefore, more cladding material is spread, resulting in too much cladding material flowing over the edges of the bearing seat, when two layers of cladding combined with 15 mm cladding width are used (Figure 26). When comparing simulation and experimental results for this parameter combination, the deviation in geometry is visually apparent. As for the experimental results, the cladding material gushed over the edge of the bearing seat, forming a curvilinear tail (Figure 26). In the corresponding simulation, the cladding material remains completely within the borders of the bearing seat. No significant amount of cladding material is distributed over to the next shaft segment.

Even though this amount of cladding material would not be considered for future investigations due to its wastefulness, the accuracy of the simulation models needed to be confirmed. Therefore, simulations with even more cladding material were calculated to see at which point the simulation diverges from the experimental findings. For this, additional hybrid work pieces were welded. This time, the diameter of the base cylinder was set to 29 mm and the cladding width to 20 mm. The simulation was again analyzed at 1.25 s of process time.

The cladding material distribution is similar between simulation and experiment (Figure 30) for 29_20_3S work pieces at 1.25 s process time. To investigate this, more simulations were calculated, varying only the cladding material width in 1 mm steps between 15 and 20 mm. The base cylinder diameter was set to 27 mm (Figure 31).

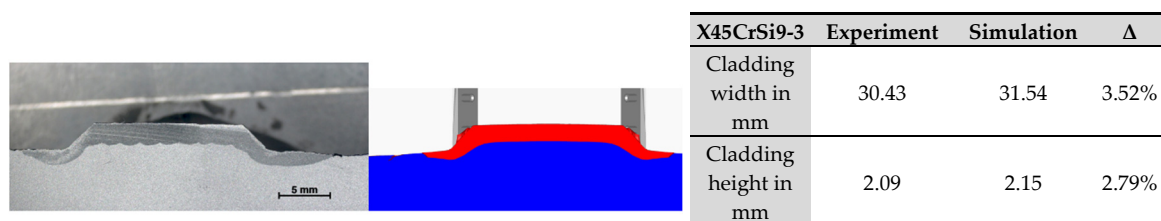


Figure 30. Comparison experiment/simulation; 29 mm base cylinder, 20 mm cladding width, 3 layers.

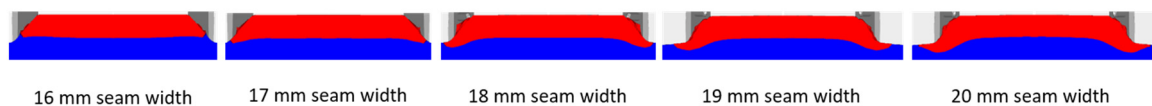


Figure 31. Different amount of cladding material resulting in differently shaped bearing seat material distribution at 1.25 s process time.

To further investigate possible reasons for the simulation model not fitting experimental results for certain amounts of cladding material, the cladding distribution was analyzed for different time steps of the simulation to ensure the simulation had been calculated to a sufficient process duration. Figure 32 shows the cladding material distribution for a 29_15_2S work piece over time as simulation output. It can be shown that the cladding material changes its shape over time during the CWR process. Whereas the cladding material of work pieces with small amounts of cladding material, e.g., 27_8_1S, remains within the bearing seat and is fully formed after 1.25 s of process time, the large cladding material amounts of the 29_15_2S work piece continue to change shape with further work piece rotations (Figure 32).

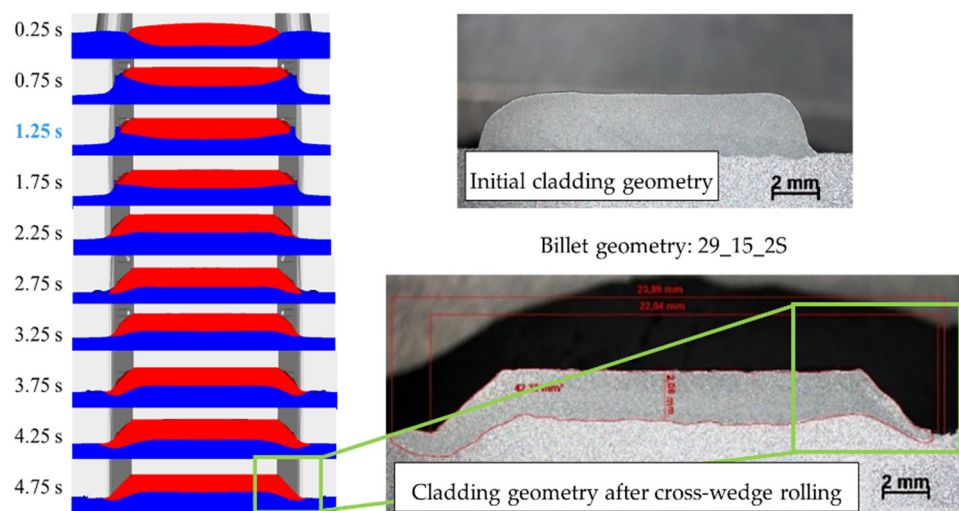


Figure 32. Analysis of cladding material distribution during cross-wedge rolling over time—cladding material X45CrSi9-3 (red) on C22.8 (blue).

The reason for this behavior becomes clear when inspecting the cross-section of the bearing seat segment of the shaft during forming at different process time steps within the simulation (Figure 33).

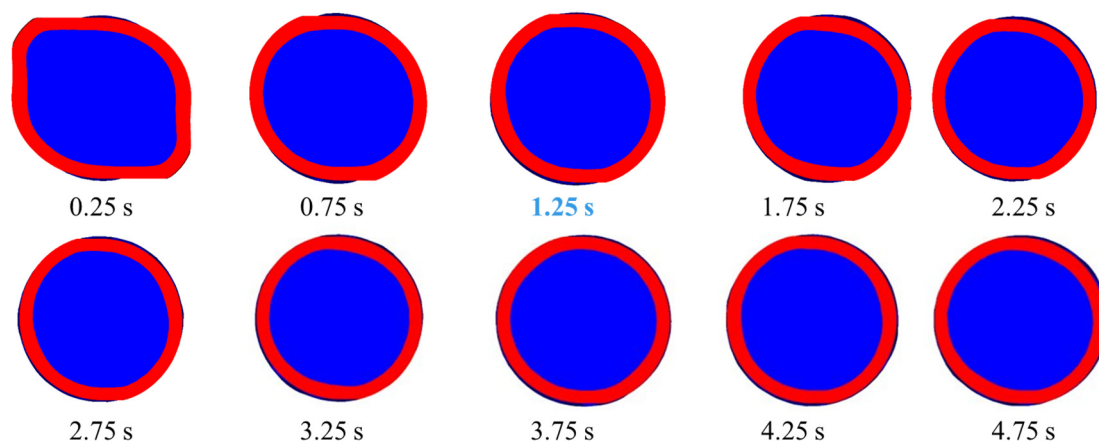


Figure 33. Over time analysis of the cladding material distribution within the cross-section of the work piece during cross-wedge rolling—cladding material X45CrSi9-3 (red) on C22.8 (blue).

At the beginning of the forming process, right after the closing of the tools, the work piece is deformed from a cylindrical shape to an ellipsoid shape (~0.25 s, Figure 33). This is intended to increase the degree of deformation to improve the material properties of the cladding material after the forming process. For small amounts of cladding material, mainly the cladding itself is deformed and the base cylinder remains a cylindrical shape. Due to the large amount (≥ 15 mm width) of cladding material, the whole bearing seat segment becomes deformed. For work pieces with 8 mm cladding width, 1.25 s process time was sufficient to return the work piece to a cylindrical shape in the area of the bearing seat after the initial upsetting. This results in more work piece rotations necessary to completely shape the bearing seat cladding. Therefore, when calculated to a further process time, the simulation model is sufficient again (Figure 32). Additionally, incorrect insertion of work pieces in the CWR module can result in unsymmetrical cladding distribution. If the influence of the work piece positioning is to be investigated, a non-symmetric simulation setup will be required. Then, even incorrectly inserted work pieces could be simulated with high accuracy, as Figure 34 qualitatively shows.

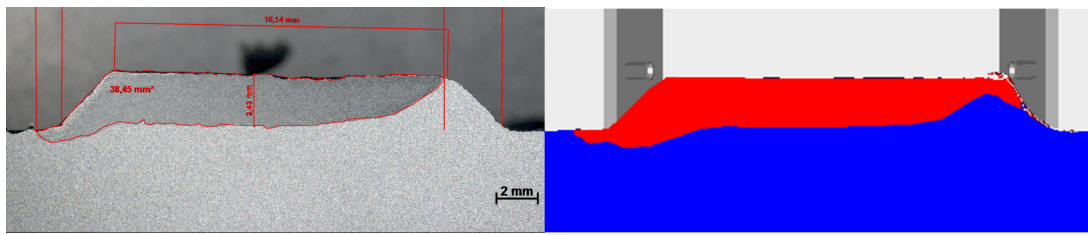


Figure 34. Unsymmetrical cladding distribution (experiment left, simulation right) due to positioning error.

When comparing the deviations between the different cladding geometries, especially the height, several influences can be identified. As shown in Figure 19 to Figure 29, the overall shape of the cladding material distribution is comparable, although the cladding height deviates more than 30% in some cases (e.g., 100Cr6). To analyze the effects of the initial work piece geometry on the cladding height deviation, the standardized and main effects were determined (Figure 35). It can be seen that the diameter of the work piece’s base cylinder has a significant effect on the deviation between simulation and experiment with regard to the cladding height (Figure 35a). The combination of seam height and seam width (total cladding volume) has less but still significant effect. The seam width alone has barely any effect, and the seam height by itself is not significant at all. Figure 35b shows that with increasing base cylinder diameter, the deviation also increases. The deviation also increases for the higher seam widths. This can be explained by more material spreading out from the bearing seat area of the work piece. The more that material is kneaded and spread out from the center part of the work piece, the larger the deviation between simulation and experiment becomes. This is analog to the previous findings, where a larger amount of cladding material resulted in larger geometry deviations (Figure 32).

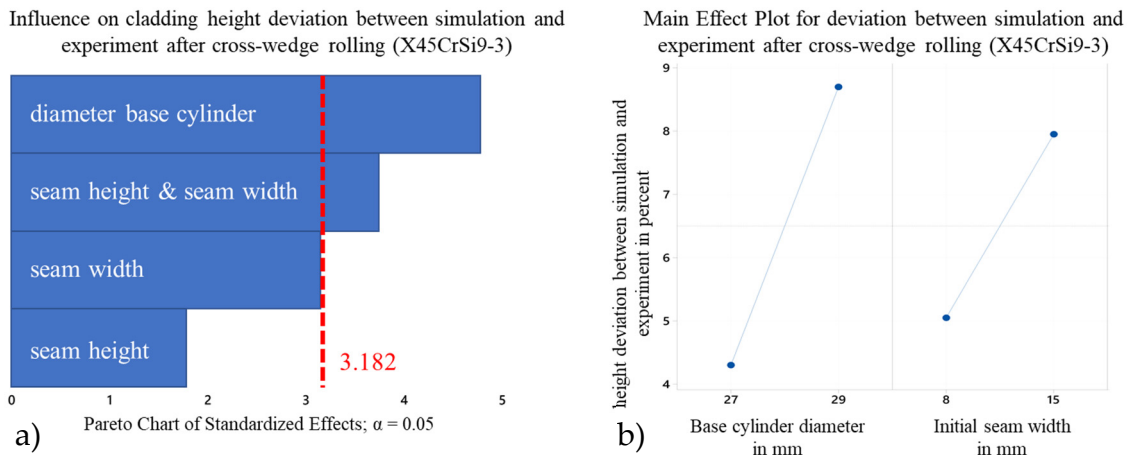


Figure 35. Influence of the cladding material amount on the accuracy of the simulation (X45CrSi9-3); (a) Pareto chart of standardized effects, (b) Main effect plot for simulation and experiment deviation

Since only the width of the seam was varied for the 100Cr6 work pieces, the approach to deviation comparison is different. Figure 27 to Figure 29 show that for 10 mm of cladding material width, the cladding height deviates more between simulation and experiment than it does in the case of larger cladding widths and therefore cladding volume.

Figure 36 shows the influence of the cladding material volume on the deviation between simulation and experiment. When the cladding material geometries of the 100Cr6 and the X45CrSi9-three work pieces are compared, it is obvious that the 100Cr6 has experienced less forming, and the cladding is not spread as wide as on the X45CrSi9-3. This can be explained by the higher flow curves of the 100Cr6 welding material compared to the database material stored in Forge NxT. Due to this, simulations

with flow curves of the actual welding material should be considered in the future to improve FEA prediction accuracy.

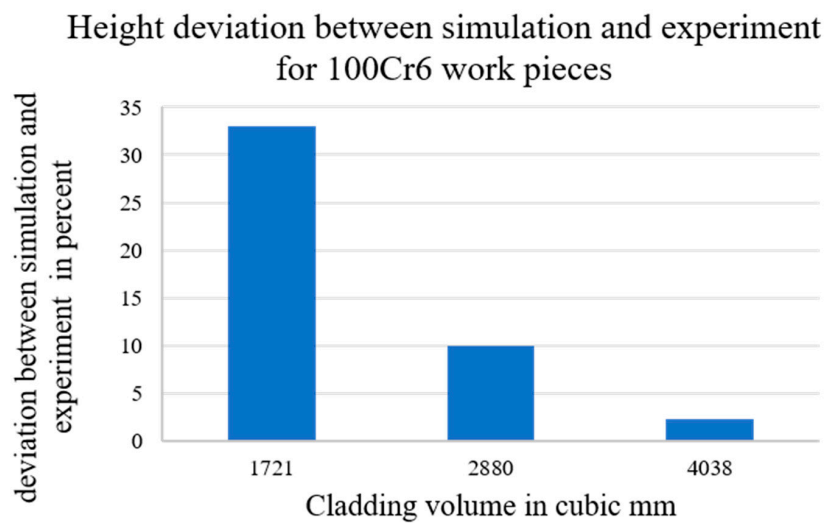


Figure 36. Influence of the cladding material amount on the accuracy of the simulation (100Cr6).

4. Discussion and Conclusions

When comparing experiments with simulation results of the cross-wedge rolling process of hybrid material work pieces, it is not sufficient to analyze only the first seconds of the forming process. Even though the axial material shifting by the wedges is technically over after the first rotation, there is still axial material flow due to excess volume remaining within the bearing seat area when using work pieces with too much cladding material. The takeaway from this would be that the time of the process simulated should be adapted to the cylindrical shape of the work piece. Only when the bearing seat is cylindrical within the simulation have the calculations progressed far enough to make a statement about the cladding distribution. When the whole process was computed, which takes almost 10 times longer than the first 1.25 s of the process, an accurate prediction of the cladding material distribution could be made. Since such a large amount cladding material would not be used for this application, such long calculation times are not something to consider. For smaller amounts of X45CrSi9-3 cladding material, the simulation model is sufficient and the method of cladding material thickness prediction is valid. For 100Cr6, more detailed simulations with more variations should be carried out. Considering that these were the first investigations with this not conventionally weldable material, the results are reasonably good.

It could be shown that the simulation results of cross-wedge rolling with coaxially arranged hybrid work pieces are in good agreement with the experimental results. In previous work, the basic suitability of the simulations for serially arranged work pieces [32] or work pieces with constant cladding thickness [37] but varied process parameters were investigated. Building on these findings, the research in this work concludes the investigations with regard to “if” and “how accurately” these multi-material simulations can predict the material flow during cross-wedge rolling. These numerical predictions of material flow can be used to weld work pieces with exact amounts of cladding materials to save material and ensure optimal layer thickness within the functional area of the part.

Too much cladding results in wasted material after machining. The goal would be to use as little cladding material as possible but enough to ensure optimal service life of the part. Which amount of cladding material will result in optimal service life of the part will be investigated in further research.

Further simulations will be carried out with flow curves taken from actual welded cladding material. Currently, specimens are being prepared in order to carry out material characterization for every material used within the research project. This will help to improve the simulation model’s accuracy even more.

Author Contributions: Conceptualization, J.K. and A.B.; formal analysis, J.K., L.B., M.Y.F., and A.B.; investigation, J.K., L.B., and M.Y.F.; methodology, J.K., M.M., L.B., T.C., and M.Y.F.; project administration, M.S., T.H., and F.P.; software, J.K.; supervision, M.S., T.H., L.O., and G.P.; validation, J.K., M.M., L.B., and M.Y.F.; visualization, J.K., L.B., T.C., and M.Y.F.; writing—original draft, J.K., L.B., T.C., and M.Y.F.; writing—review and editing, M.M., M.S., T.H., F.P., M.L., J.H., S.K., L.O., and G.P. All authors have read and agreed to the published version of the manuscript.

Funding: This research was funded by the Deutsche Forschungsgemeinschaft (DFG, German Research Foundation)—CRC 1153, subproject B1, A4, C3, T1—252662854.

Conflicts of Interest: The authors declare no conflict of interest.

References

- Mohamed, A.; Celik, T. An integrated knowledge-based system for alternative design and materials selection and cost estimating. *Expert Syst. Appl.* **1998**, *14*, 329–339. [[CrossRef](#)]
- Ljungberg, L.Y.; Edwards, K.L. Design, materials selection and marketing of successful products. *Mater. Des.* **2003**, *24*, 519–529. [[CrossRef](#)]
- Zhou, C.-C.; Yin, G.-F.; Hu, X.-B. Multi-objective optimization of material selection for sustainable products: Artificial neural networks and genetic algorithm approach. *Mater. Des.* **2009**, *30*, 1209–1215. [[CrossRef](#)]
- Sirisalee, P.; Ashby, M.F.; Parks, G.T.; Clarkson, P.J. Multi-criteria material selection in engineering design. *Adv. Eng. Mater.* **2004**, *6*, 84–92. [[CrossRef](#)]
- Bandyopadhyay, A.; Heer, B. Additive manufacturing of multi-material structures. *Mater. Sci. Eng. R Rep.* **2018**, *129*, 1–16. [[CrossRef](#)]
- Gouker, R.M.; Gupta, S.K.; Bruck, H.A.; Holzschuh, T. Manufacturing of multi-material compliant mechanisms using multi-material molding. *Int. J. Adv. Manuf. Technol.* **2006**, *30*, 1049–1075. [[CrossRef](#)]
- Merklein, M.; Johannes, M.; Lechner, M.; Kuppert, A. A review on tailored blanks—Production, applications and evaluation. *J. Mater. Process. Technol.* **2014**, *214*, 151–164. [[CrossRef](#)]
- Irving, B. Blank welding forces automakers to sit up and take notice. *Weld. J.* **1991**, *70*, 39–45.
- Saunders, F.I.; Wagoner, R.H. Forming of tailor-welded blanks. *Metall. Mater. Trans. A* **1996**, *27*, 2605–2616. [[CrossRef](#)]
- Behrens, B.-A.; Overmeyer, L.; Barroi, A.; Frischkorn, C.; Hermsdorf, J.; Kaieler, S.; Stonis, M.; Huskic, A. Basic study on the process combination of deposition welding and subsequent hot bulk forming. *Prod. Eng.* **2013**, *7*, 585–591. [[CrossRef](#)]
- Nguyen-Schäfer, H. Contact stresses in rolling bearings. In *Computational Design of Rolling Bearings*; Springer International Publishing: Cham, Switzerland, 2016. [[CrossRef](#)]
- Harris, T.A.; Barnsby, R.M. Life ratings for ball and roller bearings. *Proc. Inst. Mech. Eng. Part J J. Eng. Tribol.* **2001**, *215*, 577–595. [[CrossRef](#)]
- Hertz, H. Ueber die Berührung fester elastischer Körper. *Journal für die Reine und Angewandte Mathematik* **1882**, *92*, 156–171. [[CrossRef](#)]
- Belyaev, N.M. Local stresses in compression of elastic bodies. *Inzhenernye Sooruzheniya i Stroitel'naya Mekhanika* **1924**, 27–108.
- Sadeghi, F.; Jalalahmadi, B.; Slack, T.S.; Raje, N.; Arakere, N.K. A Review of Rolling Contact Fatigue. *ASME J. Tribol.* **2009**, *131*, 041403. [[CrossRef](#)]
- Palmgren, A.; Lundberg, G. Dynamic Capacity of Rolling Bearings. *Acta Polytech. Mech. Eng. Ser.* **1947**, *1*, 7.
- Zwirlein, O.; Schlicht, H. Werkstoffanstrengung bei Walzbeanspruchung—Einfluss von Reibung und Eigenspannungen. *Materialwissenschaft und Werkstofftechnik* **1980**, *11*, 1–14. [[CrossRef](#)]
- Förster, R.; Förster, A. *Einführung in die Fertigungstechnik*; Springer Vieweg: Berlin, Germany, 2018; p. 130. [[CrossRef](#)]
- Schuler, V.; Twrdek, J. *Praxiswissen Schweißtechnik: Werkstoffe, Prozesse, Fertigung*, 6th ed.; Springer Vieweg: Wiesbaden, Germany, 2019; p. 268. ISBN 978-3-658-24266-4.
- Kottman, M.; Zhang, S.; McGuffin-Cawley, J.; Denney, P.; Narayanan, B.K. Laser Hot Wire Process: A Novel Process for Near-Net Shape Fabrication for High-Throughput. *JOM J. Miner. Met. Mater. Soc.* **2015**, *67*, 622–628. [[CrossRef](#)]
- Liu, S.; Liu, W.; Kovacevic, R. Experimental investigation of laser hot-wire cladding. *Proc. Inst. Mech. Eng. B J. Eng.* **2017**, *231*, 1007–1020. [[CrossRef](#)]

22. Nowotny, S.; Brueckner, F.; Thieme, S.; Leyens, C.; Beyer, E. High-performance laser cladding with combined energy sources. *J. Laser Appl.* **2015**, *27*, 1–7. [[CrossRef](#)]
23. Lostado Lorza, R.; Escribano García, R.; Fernandez Martinez, R.; Martínez Calvo, M.Á. Using Genetic Algorithms with Multi-Objective Optimization to Adjust Finite Element Models of Welded Joints. *Metals* **2018**, *8*, 230. [[CrossRef](#)]
24. Blohm, T.; Nothdurft, S.; Mildebrath, M.; Ohrdes, H.; Richter, J.; Stonis, M.; Langner, J.; Springer, A.; Kaierle, S.; Hassel, T.; et al. Investigation of the joining zone of laser welded and cross wedge rolled hybrid parts. *Int. J. Mater. Form.* **2018**, *11*, 829–837. [[CrossRef](#)]
25. Coors, T.; Hwang, J.-I.; Pape, F.; Poll, G. Theoretical investigations on the fatigue behavior of a tailored forming steel-aluminium bearing component. *AIP Conf. Proc.* **2019**, *2113*, 040020. [[CrossRef](#)]
26. Coors, T.; Pape, F.; Poll, G. Bearing Fatigue Life of a Multi-Material Shaft with an Integrated Raceway. *Bear. World J.* **2018**, *3*, 23–30.
27. Matthes, K.; Schneider, W. *Schweißtechnik—Schweißen von Metallischen Konstruktionswerkstoffen*, 6th ed.; Hanser Verlag: München, Germany, 2016; pp. 33–34. ISBN 978-3446405684.
28. Dilthey, U. *Schweißtechnische Fertigungsverfahren 2—Verhalten der Werkstoffe beim Schweißen*, 3rd ed.; Springer: Berlin, Germany, 2005; p. 130. ISBN 978-3-540-27402-5.
29. Lammers, M.; Budde, L.; Barroi, A.; Hermsdorf, J.; Kaierle, S. Entwicklung von Laser-Systemkomponenten optimiert für die additive Serienfertigung mittels SLM. In *Konstruktion für die Additive Fertigung*, 1st ed.; Lachmayer, R., Lippert, R.B., Kaierle, S., Eds.; Springer Vieweg: Berlin/Heidelberg, Germany, 2020; pp. 21–35. [[CrossRef](#)]
30. Pajukoski, H.; Näkki, J.; Thieme, S.; Tuominen, J.; Nowotny, S.; Vuoristo, P. High performance corrosion resistant coatings by novel coaxial cold- and hot-wire laser cladding methods. *J. Laser Appl.* **2016**, *28*, 012011. [[CrossRef](#)]
31. Pater, Z. Cross-Wedge Rolling. In *Comprehensive Materials Processing 13 Volume Set*, 1st ed.; Hashmi, S., Batalha, G.F., van Tyne, C.J., Yilbas, B., Eds.; Elsevier: Amsterdam, The Netherlands, 2014; Volume 3. [[CrossRef](#)]
32. Kruse, J.; Jagodzinski, A.; Langner, J.; Stonis, M.; Behrens, B.-A. Investigation of the joining zone displacement of cross-wedge rolled serially arranged hybrid parts. *Int. J. Mater. Form.* **2019**, *13*, 577–589. [[CrossRef](#)]
33. Pater, Z.; Tomczak, J.; Bulzak, T. New forming possibilities in cross wedge rolling processes. *Arch. Civ. Mech. Eng.* **2018**, *18*, 149–161. [[CrossRef](#)]
34. Pater, Z.; Tomczak, J.; Bulzak, T.; Wójcik, Ł.; Lis, K. Rotary compression in tool cavity—A new ductile fracture calibration test. *Int. J. Adv. Manuf. Technol.* **2020**, *106*, 4437–4449. [[CrossRef](#)]
35. Transvalor, S. *A Reference Documentation; FORGE@NxT 3.0*; Transvalor: Biot, France, 2019.
36. Hensel, A.; Spittel, T. *Kraft- und Arbeitsbedarf Bildsamer Formgebungsverfahren*, 1st ed.; Deutscher Verlag für Grundstoffindustrie: Leipzig, Germany, 1978.
37. Jagodzinski, A.; Kruse, J.; Barroi, A.; Mildebrath, M.; Langner, J.; Stonis, M.; Lammers, M.; Hermsdorf, J.; Hassel, T.; Behrens, B.-A.; et al. Investigation of the Prediction Accuracy of a Finite Element Analysis Model for the Coating Thickness in Cross-Wedge Rolled Coaxial Hybrid Parts. *Materials* **2019**, *12*, 2969. [[CrossRef](#)]

